Chapter 8
Thermoelectric Properties of Metal Chalcogenides Nanosheets and Nanofilms Grown by Chemical and Physical Routes

Ananya Banik, Suresh Perumal, and Kanishka Biswas

8.1   Introduction

To alleviate the vivid surge of the worldwide energy crisis, furnishing renewable, sustainable and environment-friendly energy source holds precedence not only to the scientific community yet added to the overall populace all in all [1–3]. Thermoelectric (TE) materials are gaining attention in this area because of their ability in waste heat to electricity conversion [1]. The efficiency of any thermoelectric material is governed by the thermoelectric figure of merit, zT, which is the function of electrical conductivity (σ), Seebeck coefficient (S), total thermal conductivity (κ_{total}) and temperature (T) via the expression, $zT = \sigma S^2 T/\kappa_{total}$ [3]. The quantity σS^2 is called power factor (PF). κ_{total} of a material depends on electronic (κ_{el}) and lattice (κ_{lat}) thermal conductivity ($\kappa_{total} = \kappa_{el} + \kappa_{lat}$). A high performance thermoelectric material should have all together high electrical conductivity (σ) to minimize the internal Joule heating, a large Seebeck coefficient

A. Banik
New Chemistry Unit, Jawaharlal Nehru Centre for Advanced Scientific Research (JNCASR), Bangalore, India

S. Perumal
Department of Physics and Nanotechnology, SRM Institute of Science and Technology, Chennai, Tamil Nadu, India

K. Biswas (✉)
New Chemistry Unit, Jawaharlal Nehru Centre for Advanced Scientific Research (JNCASR), Bangalore, India

School of Advanced Materials, Jawaharlal Nehru Centre for Advanced Scientific Research (JNCASR), Bangalore, India

International Centre for Materials Science, Jawaharlal Nehru Centre for Advanced Scientific Research (JNCASR), Bangalore, India
e-mail: kanishka@jncasr.ac.in

(S) to generate high voltage and low thermal conductivity (κ_{total}) to maintain the temperature gradient. However, the major challenge relies on the improvement of the material's thermoelectric performance involving the optimization of these three interdependent material properties [2].

During the last decade various novel strategies have been introduced to decouple these interrelated physical parameters [2, 4, 5]. Approaches to improve the power factor (σS^2) include band convergence [6, 7], minority carrier filtering [8], quantum confinement effect [9–11] and formation of sharp impurity states close to Fermi level to increase density of states (DOS) [12]. To block the thermal transport for maintaining temperature difference across a given material/device, increased phonon scattering can be achieved by introducing mass-fluctuation [13, 14], nanostructuring [15, 16], creating the hierarchical nano/meso-scale architectures [17] and intrinsic bond anharmonicity [18, 19]. However, the highest reported zT value is still below 3, which limits the usage of thermoelectric energy conversion to niche applications [20]. Low dimensional materials exhibit combination of both the enhancement in power factor due to quantum confinement effect, wherein flow of charge carriers is restricted and placed in a potential well with infinitely high walls, and the increased phonon scattering, led to significantly low thermal conductivity, by a large number of interfaces and grain boundaries [11, 21]. Confinement in the dimensionality significantly distorts the density of states of a given material and introduces the large interfaces that scatter phonon effectively rather than electrons and reduces the thermal conductivity drastically. For instance, Fig. 8.1a illustrates the schematic diagram of 3D (bulk), 2D (quantum well), 1D (quantum wire) and 0D (quantum dot) solid. Their corresponding DOS is given in Fig. 8.1b. In low dimensional systems, the thermoelectric parameters, such as S, σ and κ_{total} can be effectively tailored independently. Previous literature reports revealed that ultrathin nanosheets and nanofilms can exhibit enhanced densities of states (DOS) and carrier mobility (μ) compared with their bulk counterparts [22]. Significant increment in Seebeck coefficient has been achieved for n-type PbTe/Pb$_{0.927}$Eu$_{0.073}$Te multiple quantum wells (MQW) as compared to bulk PbTe material [10], which is consistent with theoretical calculations, as shown in Fig. 8.1c. A zT of 0.9 at 300 K and 2.0 at 550 K have been achieved in PbSe$_{0.98}$Te$_{0.02}$/PbTe quantum-dot structures [23, 24]. Further, the theoretical calculations suggested that Bi$_2$Te$_3$-based quantum well (2D) and quantum wire 1D materials would exhibit extremely high zT as compared to bulk materials due to quantum confinement induced remarkable enhancement in power factor and large interfaces driven low thermal conductivity. Figure 8.1d presents the exponential increase in zT of Bi$_2$Te$_3$ with decrease in thickness or diameter of quantum well (or quantum wire), respectively [9–11, 25, 26]. Thin film superlattices structures utilize the acoustic mismatch between the superlattice components to reduce κ_{lat} while retaining the electrical transport intact (phonon-blocking/electron-transmitting) [24]. These result in high thermoelectric performance which is rather impossible using the conventional alloying approach, thereby potentially eliminating alloy scattering of carriers [5].
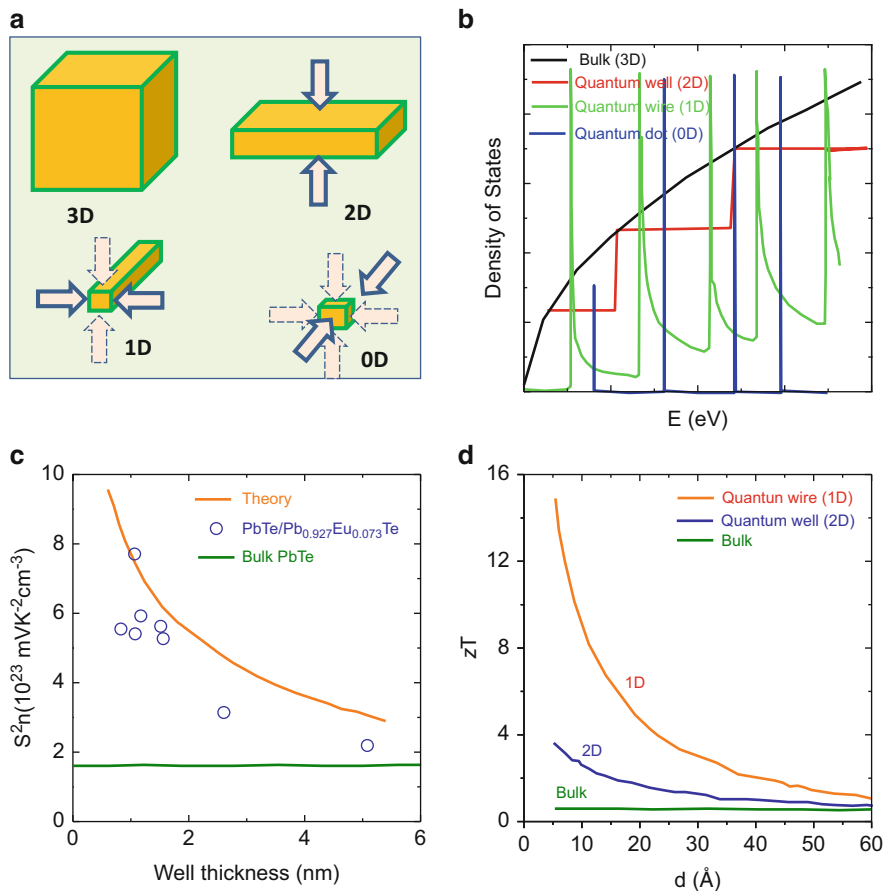
Fig. 8.1 (**a**) Schematic diagram of 3D (bulk), 2D (quantum well), 1D (quantum wire) and 0D (quantum dot) solid. (**b**) DOS vs. E plot for 3D, 2D, 1D and 0D, (**c**) the plot of $S^2 n$ vs. well thickness for n-type PbTe/Pb$_{0.927}$Eu$_{0.073}$Te multiple quantum wells (MQW) at 300 K, (**d**) calculated zT as a function of thickness/diameters of 3D, 2D and 1D for Bi$_2$Te$_3$-based materials [9–11]

8.2 Thermoelectric Transport Mechanism in Nanosheets

Ideas in using nanosheets (nanofilms) to progress the field of thermoelectrics through the enhancement of electrical conductivity and reduction of thermal conductivity were first discussed by Dresselhaus, Harman and Venkatasubramanian [4]. According to the Hicks−Dresselhaus model [11, 27], Seebeck coefficient for quantum-well structures increases linearly with decreasing the material thickness because of the quantum confinement effect, where S is directly proportional to the energy derivative of the density of states (DOS) at the Fermi level (E_F) (Mott–Jones relation, Eq. (8.1)) [11, 28].

$$S = \frac{\pi^2}{3} \frac{k_B}{q} k_B T \left\{ \frac{d\left[\ln\left(\sigma\left(E\right)\right)\right]}{dE} \right\}_{E=E_F} \tag{8.1}$$

$$= \frac{\pi^2}{3} \frac{k_B}{q} k_B T \left\{ \frac{1}{n} \frac{dn(E)}{dE} + \frac{1}{\mu} \frac{d\mu(E)}{dE} \right\}_{E=E_F}$$

$$S = \frac{8\pi^2 k_B^2}{3eh^2} m_d{}^* T \left(\frac{\pi}{3n}\right)^{2/3} \tag{8.2}$$

$$m_d{}^* \alpha \left[\frac{g(E)}{\left(\sqrt{2E}\right)} \right]^{3/2} \tag{8.3}$$

Here, k_B is the Boltzmann constant, h is the Planck constant, $m_d{}^*$ is the density of state effective mass of carriers, n is the carrier concentration and T is the absolute temperature. From Eq. (8.1), it is clear that S can be enhanced via the two mechanisms, (1) energy-dependence of carrier density, $n(E)$ and (2) energy-dependence of mobility, $\mu(E)$. Here $n(E)$ is associated with density of states, $g(E)$ $n(E) = g(E) f(E)$, where $g(E)$ is the DOS per unit volume and per unit energy; $f(E)$ is the Fermi function, whereas $\mu(E)$ depends on the energy of the charge carriers. As the best TE material falls under degenerate semiconductors, change in density of state, $g(E)$, has a direct consequence of the change in density of state effective mass $(m_d{}^*)$ which significantly alters the Seebeck coefficient, as per Eqs. (8.2) and (8.3).

The enhancement of the Seebeck coefficient of nanosheet (nanofilm) sample originates from the steplike $n(E)$, where $g(E)$ can be improved via carrierpocket engineering. The anisotropic nature of the band structure offers a possibility of tuning the relative contributions of different carrier pockets near the Fermi surface by changing the several parameters, such as the growth direction. The sharp rise in the local DOS leads to an escalation in the Seebeck coefficient with minimal change in the carrier concentration, thus decoupling the electrical conductivity and the Seebeck coefficient [29, 30]. Hence, true atomic thickness would create a two-dimensional (2D) electron gas in the single layer, which would improve S for the ultrathin layered materials [22]. Furthermore, the potential barriers at the interfaces and boundaries of the nanofilm would be expected to filter out low-energy carriers (cold carriers) and transmit high-energy carriers (hot carriers), resulting in a further increased S [31]. This high carrier mobility derived from the electronic structure has a negligible impact on phonon transport. Therefore, the μ/κ_{lat} values of a nanosheets are always much higher than those of bulk materials [5]. Furthermore, the presence of the enormous grain boundaries and interfaces in the nanofilms scatters short/mid/long-wavelength phonons, thus contributing to

a decrease in κ_{lat} with a minimal detrimental effect on the electrical properties [22]. Inorganic nanosheets usually exhibit surface structural disorder, allowing for efficient scattering of short-wavelength phonons, which decreases κ_{lat}.

Moreover, the thin film interfaces influence both in-plane and out-of-plane thermal conductivity [5]. Interface effects can be classified into three categories: specular, diffuse and hybrid (partially specular and partially diffuse). At a specular interface, phonons transport (transmitted or reflected) at the layer interface following Snell's law, when polarization changes are neglected [32]. When the incident angle is beyond a critical angle, the phonons should reflect totally and not cross the interface. At a diffuse interface, the thermal conductivity along the layers is irrelevant to the transmissivity and reflectivity. Therefore, the thermal transport properties can be estimated from the individual layers separately. However, at a hybrid interface, the energy flux of phonons between layers due to the transmissivity cannot be ignored. Here, the partial diffusion behaves as a barrier to weaken the continuity between layers. Nanosheets always possess partially specular and partially diffuse interfaces. Thus, the atomic-scale roughness is thought to be one of the main reasons for the reduction in the thermal conductivity of nanosheets materials. Considering that these mechanisms will not affect the carrier mobility, nanosheets have been regarded as one of the best materials to achieve the "phonon glass electron crystal" criterion [5].

8.3 Thin Films of Layered Chalcogenides Prepared by Physical Route

Bi_2Te_3-based systems have been well known for their superior TE properties even in the nanostructured bulk form [27]. Though many TE materials have been studied with considerably good TE performance, Bi_2Te_3-based alloys have been recognized as the state-of-the-art TE materials for room and/or low temperature applications [33]. In this part, we extensively discuss a unique structure of Bi_2Te_3 and the influence of physical deposition techniques and annealing temperature on TE properties of Bi_2Te_3-based thin films. The Bi_2Te_3 crystallizes in the rhombohedral crystal structure with the space group of R-3m with the lattice constant in the *c*-axis (30.48 Å) is much higher than that of the *a*, *b*-axis (4.38 Å). Presence of unique structural anisotropy in Bi_2Te_3 leads to large carrier mobility and electrical conductivity along *ab*-plane as compared to *c*-axis [29, 34]. Further, it has a hexagonal layered structure with stacking of quintuple layers of covalently bonded Te(1)–Bi–Te(2)–Bi–Te(1); each quintuple layer is connected by the weak van der Waals interactions [35].

The deposition of Bi_2Te_3-based films can be performed by various physical deposition techniques such as sputtering (magnetron/RF magnetron/co-sputtering/ion beam), evaporation (thermal/e-beam/flash), pulsed laser deposition (PLD) and molecular beam epitaxy (MBE) [36–49]. Among them, every technique has its

own advantages and disadvantages. As is known, transport properties of thin films prepared by physical deposition techniques mostly depend on composition, crystal structure, substrate temperature, Te and Bi defects, annealing temperature, decomposition or evaporation rate of starting elements and even deposition techniques for some extent. In case of thermoelectric properties, thin film metrology also plays a key role as in-plane measurement of S, σ and κ_{total} is slightly easier than measurement in out of plane, where maintaining temperature difference is of great challenge. Thus, most of the research groups work on thin film-based thermoelectrics and report mostly the electronic-transport properties, such as S, σ and σS^2 due to challenge in the measurement of thermal conductivity. As TE properties strongly depend on the composition of materials, it is important to control an evaporation rate of Bi, Sb and Te during deposition of Bi_2Te_3 and $Bi_{2-x}Sb_xTe_3$-based thin films since Te, Bi and Sb possess different vapour pressures. Thus, reports showed that Te content in 60–65 at% gives an optimum composition of Bi_2Te_3, comparable with initial composition, with reasonably high zT [42–44].

Further thickness dependent thermoelectric properties of Bi_2Te_3-based thin films were also studied in detail as thick of the films will effectively control the transport properties. It has been further reported that co-evaporation method can be an efficient route to prepare Bi_2Te_3-based materials where evaporation rate of both Bi and Te can be simultaneously controlled during deposition, and nominal composition with optimum thickness could also be maintained. Deposition methods with the nominal composition of Bi_2Te_3-based materials and their corresponding thermoelectric properties are listed in Table 8.1. When compared to all other techniques co-evaporation and co-sputtering techniques seem to have better composition control and thereby notable high TE figure of merits, zTs of 0.91 and 0.81 for n-type Bi_2Te_3, 0.87 [48, 49, 57] for p-type $Bi_{0.5}Sb_{1.5}Te_3$. Nevertheless, p-type Bi_2Te_3/Sb_2Te_3 superlattices with individual layers of 10 Å prepared by low-temperature growth process have still being considered a predominant material with a record-high zT of ~2.4 at 300 K [4].

Zhang et al. have successfully deposited the (00l) oriented Bi_2Te_3 thin films by magnetron co-sputtering method and compared with ordinary film and bulk target materials [51]. They have achieved the maximum power factor (σS^2) of 33.7 μW/cmK^2 at 360 K which is four times higher than the ordinary film and notably high compared to SPS sintered Bi_2Te_3 bulk material. This huge rise in σS^2 is due to the increase in mobility from ~23 cm^2/V·s (ordinary film) to ~52 cm^2/V·s for (00l) oriented Bi_2Te_3 thin film as unique anisotropy associated high mobility in ab-plane than c-axis. Further, the calculated cross-plane thermal conductivity was about 0.81 W/mK which is notably low as compared to p-type Bi_2Te_3/Sb_2Te_3 superlattices (0.95 W/mK) [4, 51]. The Bi_2Te_3 thin films with optimum 57 at% of Te content deposited on flexible polyimide substrate by vacuum thermal evaporation showed the σS^2 value of 12 μW/cmK^2 at 300 K. Moreover, the electrodeposited Bi_2Te_3-based thin films and nanowire arrays have shown the S value of −70 μV/K with σS^2 of 5.63 μW/cmK^2 [52]. The influence of deposition methods of prepared Bi_2Te_3-based thin films and the respective TE properties (σ, S and σS^2) have been illustrated in Fig. 8.2 and summarized in Table 8.2.

Table 8.1 Deposition methods, nominal composition and thermoelectric properties of n- and p-type Bi_2Te_3-based materials [50]

Composition	Method	Temp. (K)	σ ((10^4) S/m)	S (μV/K)	$S^2\sigma$ (μW/cm·K^2)
n-Bi_2Te_3 bulk target [51]	As melted	380	7.4	−130	10.8
n-Bi_2Te_3	Ordinary film	360	4	−140	7.2
n-(001) oriented Bi_2Te_3	Magnetron co-sputtering	360	8.5	−230	33.7
n-$Bi_2(Te_{0.6}Se_{0.4})_3$ [36]	Vacuum thermal evaporation	300	700	200 (473 K)	35.3
n-Bi_2Te_3 [37]	RF sputtering	300	6.74	−118.6	9.5
n-Bi_2Te_3 [38]	e-beam evaporation	300	62.5	−19	2.3
n-Bi_2Te_3 [39]	RF magnetron sputtering	300	6.6	−38	1.1
		423	6.1	−80	4
		463	4.8	−80	3
		543	4.5	−160	13
n-Bi_2Te_3 [40]	Co-sputtering	303	3.2	−50	0.8
		423	3.2	−68	1.47
		573	3.5	−89	2.77
		673	5.5	−122	8.86
	Annealed at 673 K	423 (max)	7.4	−224	32.8
n-Bi_2Te_3 [52]	Electro-deposition	300	11.49	−70	5.63
n-Bi_2Te_3	RF magnetron sputtering	300	2.5	−150	5.62
n-Bi_2Te_3 [53]	Pulsed laser deposition	300	6.6	−194	25
p-$Bi_{0.3}Sb_{1.7}Te_3$		300	9.09	200	35.1
n-Te embedded Bi_2Te_3 [54]	Molecular beam epitaxy	300	6.5	205	27.3
		473	8.25	231	44.02
		523	7.1	190	25.63
n-Bi_2Te_3 [41]	RF magnetron sputtering	323	3.2	−94	27.1
p-$Bi_{1.5}Sb_{0.5}Te_3$ [55]	Thermal evaporation (45° tilt angle)	300	8.6	262	58.6
	(60° tilt angle)		7.9	238	45.2
	(90° tilt angle)		7.5	213	33.5
p-$(Bi/Sb)_2Te_3$ [56]	Thermal evaporation (45° tilt angle)	300	8.8	246	54.2
	(60° tilt angle)		7.4	221	36.5
	(90° tilt angle)		5.1	204	21.5
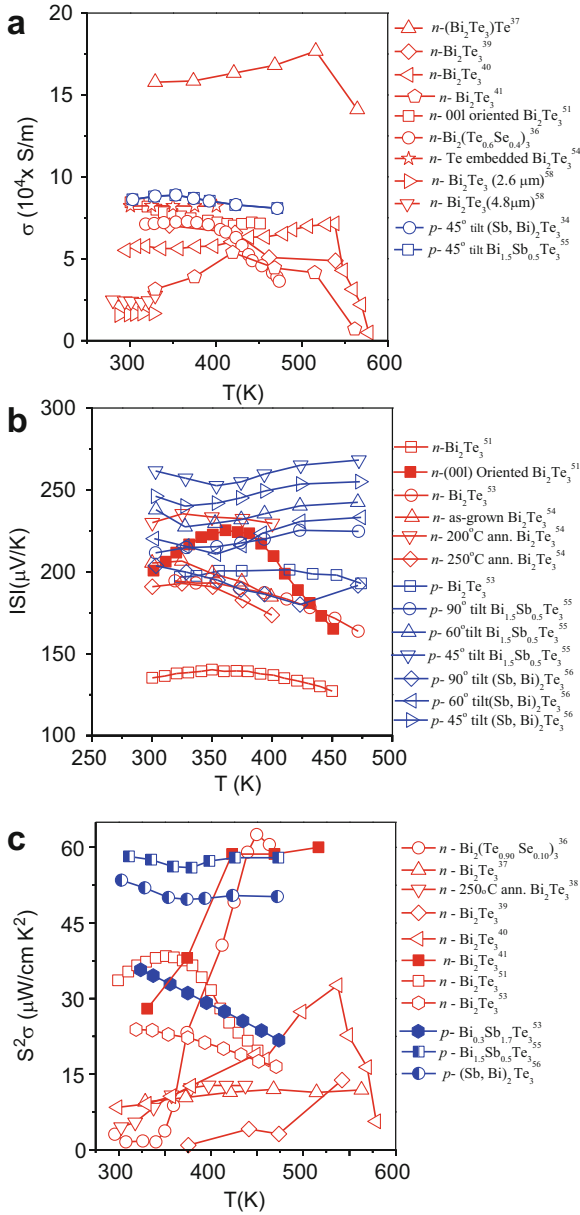
Fig. 8.2 Thermoelectric properties, (**a**) electrical conductivity (σ), (**b**) Seebeck coefficient (S) and (**c**) power factor ($S^2\sigma$) of Bi_2Te_3-based thin films deposited by various techniques

Table 8.2 Physical deposition methods, composition, applied temperature, annealing temperature and thermoelectric properties of Bi_2Te_3-based thin films [50]

Deposition methods	Composition	α ($\mu V/K$)	ρ ($\mu\Omega m$)	$S^2\sigma$ (10^{-3} W/m·K)	zT (300 K)
Co-evaporation	n-Bi_2Te_3	−228	28.3	1.8	–
Co-sputtering	n-Bi_2Te_3	−55	10	0.3	–
Co-evaporation	n-Bi_2Te_3	−220	10.6	4.57	0.91
Flash	n-$Bi_2Te_{2.72}Se_{0.3}$	−200	15	2.7	–
Sputtering	n-$Bi_{1.8}Sb_{0.2}Te_{2.7}Se_{0.3}$	−235	47	1.2	–
Co-sputtering	n-Bi_2Te_3	−160	16.3	1.6	–
Sputtering	n-$Bi_2Se_{0.3}Te_{2.7}$	−160	20	1.3	–
Co-evaporation	n-Bi_2Te_3	−228	13.0	4.0	0.81
Flash	p-$Bi_{0.5}Sb_{1.5}Te_3$	240	12	4.8	–
Co-sputtering	p-$(Bi/Sb)_2Te_3$	175	12.1	2.5	–
Flash	p-$Bi_{0.5}Sb_{1.5}Te_3$	230	17	3.1	0.87
Sputtering	p-$Bi_{0.5}Sb_{1.5}Te_3$	210	25	1.8	–

Pulsed laser deposited n-Bi_2Te_3 and p-$Bi_{0.3}Sb_{1.7}Te$ c-axis oriented thin films have shown significantly high TE performance [53]. For instance, *in*-plane measured σ, S and σS^2 of n-Bi_2Te_3 films are 6.6×10^4 S/m, -194 $\mu V/K$ and 25.2 $\mu W/cmK^2$ [58], whereas p-$Bi_{0.3}Sb_{1.7}Te$ showed σ, S and σS^2 values of 9.09×10^4 S/m, 200 $\mu V/K$ and 33.1 $\mu W/cmK^2$. Further, as annealing temperature after deposition, substrate temperature during deposition and thickness of films significantly influence the TE properties of prepared thin films, Hyejin Choi et al. have recently studied the effect of annealing temperature by controlling the each layer of Bi (3 Å) and Te (9 Å) on SiO_2/Si substrate using molecular beam epitaxial method on TE properties of Te embedded Bi_2Te_3 thin films [54]. The formed epitaxial Bi_2Te_3 thin film with heterojunctions has exhibited the maximum zT of ~2.27 at 375 K due to significant phonon scattering rather than electron scattering, led to high σ and notably low κ_{total}. In particular, as-grown Bi_2Te_3 thin film showed σ, S, $S^2\sigma$ and κ_{total} values of 6.5×10^4 S/m, 205 $\mu V/K$, 27.3 $\mu W/cmK^2$ and ~0.9 W/mK, whereas the film thus annealed at 473 K exhibited σ, S, $S^2\sigma$ and κ_{total} values of 8.25×10^4 S/m, 231 $\mu V/K$, 44.02 $\mu W/cmK^2$ and ~0.75 W/mK. It is clear that Te embedded Bi_2Te_3 nano-grain structured epitaxial thin film showed the record-high TE performance due to increased phonon scattering rather than carrier scattering at grain boundaries and interfaces.

Further, it has been shown that grown angles of the array of nanowire or bundles of deposited Bi_2Te_3 thin films also alter the TE properties. Recently, Ming Tan et al. have reported that hierarchical p-$Bi_{1.5}Sb_{0.5}Te$ nanopillar array and p-$(Bi/Sb)_2Te_3$ nanowires array with well-oriented growth prepared by vacuum thermal evaporation method with a certain tilt angle to substrate showed extremely high zTs of 1.61 and 1.72 at 300 K [55, 56]. These observed huge enhancements in zT for tilt-structure of p-$Bi_{1.5}Sb_{0.5}Te$ array are due to preferred phonon scattering than carriers scattering

in heterojunctions, and tilt-induced change in Fermi level enhances the flow of carriers and thereby σ increases drastically, which altogether supports to have high TE performance [59]. Presence of surface states at an energetic position above the conduction band edge in $(Sb,Bi)_2Te_3$ material exhibits a charge transfer from the surface state to the bulk [60]. So, electrical conductivity remarkably increases due to electron accumulation at the surface of nanowires with a high surface-to-volume ratio. This huge increase in σ from 5.1×10^4 S/m for a tilt angle of $90°$ to 9.1×10^4 S/m for a tilt-angle of $45°$ led to record-high zTs of 1.72 for c-axis oriented Bi_2Te_3 nanowire arrays (Fig. 8.2) [56].

8.4 Nanosheets of Layered Chalcogenides Synthesized by Chemical Route

Although thin-film thermoelectric materials offer tremendous scope for zT enhancement, questions remain on the precision of the zT reported due to experimental difficulties in measuring the properties correctly. Furthermore, most of the above methods require expensive apparatus and are not easy to control. Synthesis of large-area 2D metal chalcogenide thin films with controlled growth is a major challenge in this field of research. Synthesis based on the vapour processes such as molecular beam epitaxy has been successful in the preparation of large-area uniform thin films of 2D materials. However, this process requires synthesis conditions of high temperature, vacuum and specific substrates for materials growth. In addition, it is limited in the robustness of scale-up because the film growth takes a long time and the fine control of the film thickness over the entire large-size substrate is difficult. Additionally, materials fabricated by sophisticated techniques are not easily incorporated into commercial devices because they are slow and expensive to fabricate, and they cannot be fabricated in sufficient quantities. Solution phase synthesis has emerged as a promising alternative to the above-mentioned preparation technique. The solution-based process has several technological advantages: low temperature synthesis under atmospheric conditions, and more diversity in the material species to be synthesized. In the following section, we will be focusing on the thermoelectric properties of recently synthesized solution processed metal chalcogenides nanosheets.

8.4.1 Bismuth Telluride

Promising TE performance of bismuth telluride (Bi_2Te_3) thin film has motivated researchers to study TE properties of Bi_2Te_3 nanosheets. p- and n-type nanostructured bulk Bi_2Te_3-based materials with zT of 1.1 have been realized by bottom-up assembly of rapidly synthesized single-crystalline nanoplates of sulphur-doped
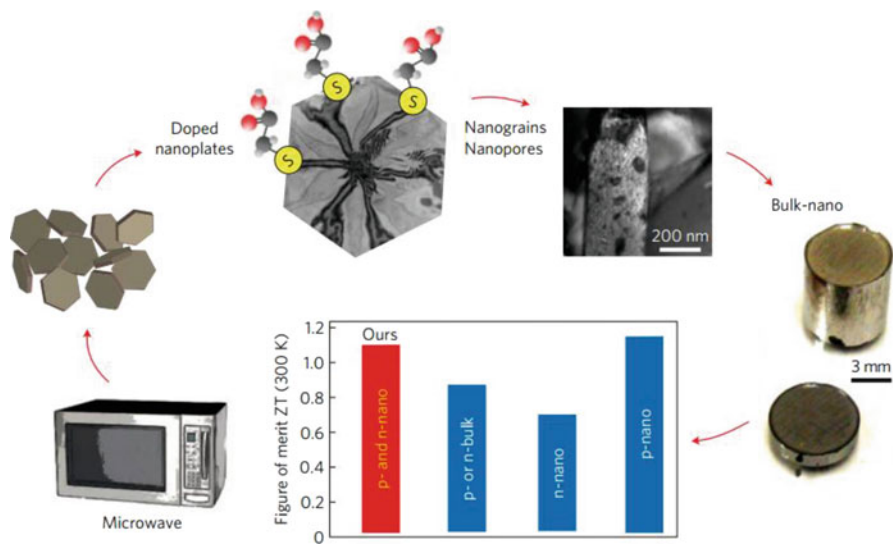
Fig. 8.3 Schematic demonstration of the scalable synthesis technique used to obtain both *n*- and *p*-type bulk thermoelectric nanomaterials $Bi_2Te_{3-x}S_x$ with high figures of merit. Microwave synthesis of $Bi_2Te_{3-x}S_x$ nanoplates followed by cold-pressing and sintering yields dense bulk pellets (density is $92 \pm 3\%$ of theoretical density) with nanostructured grains. Sulphur doping in Bi_2Te_3 optimizes the electrical conductivity, Seebeck coefficient and majority carrier type, while nanostructuring results in very low κ_{total}. The graph compares the best *ZT* ($\sim zT$) of *p*- and *n*-type nanomaterials with those of the best *p*- and *n*-bulk materials, denoted as *p*- or *n*-bulk, nanoparticle-dispersed *n*-bulk, referred to as *n*-nano, and a *p*-type ball-milled alloy, denoted as *p*-nano. Adapted with permission from Ref. [61] © 2012, Nature Publishing Group

Bi/Sb telluride [61]. Bismuth chloride ($BiCl_3$) and antimony chloride ($SbCl_3$) have been used as metal precursors in inexpensive organic solvents for rapid preparation of large amount of sulphur-doped pnictogen chalcogenide (V_2VI_3) nanosheets to prepare single- and multi-component nanostructured bulk TE materials (Fig. 8.3). Microwave stimulation enhances the rate of reaction between molecularly ligated chalcogen and pnictogen complexes with thioglycolic acid (TGA) in the presence of a high-boiling solvent. Nanostructured Bi_2Te_3 pellets showed lower lattice thermal conductivity and high power factors, comparable to its bulk counterpart. Nanostructuring and sulphur doping result in these remarkable charge-carrier-crystal and phonon-glass behaviours. Thus, Bi_2Te_3 nanosheets exhibit 250% higher *zT* than their non-nanostructured bulk counterparts and state-of-the-art alloys (Fig. 8.3).

Spark plasma sintering (SPS) is well known to be a very useful technique for preparation of nanostructured bulk TE materials because of its fast heating and cooling rates, which allow rapid sintering, avoid undesirable grain growth emerging from a long sintering process at high temperatures. The grain growth can be manipulated by varying the SPS conditions, allowing to study the effect of grain size and density on the TE properties of nanostructured bulk materials. Recently
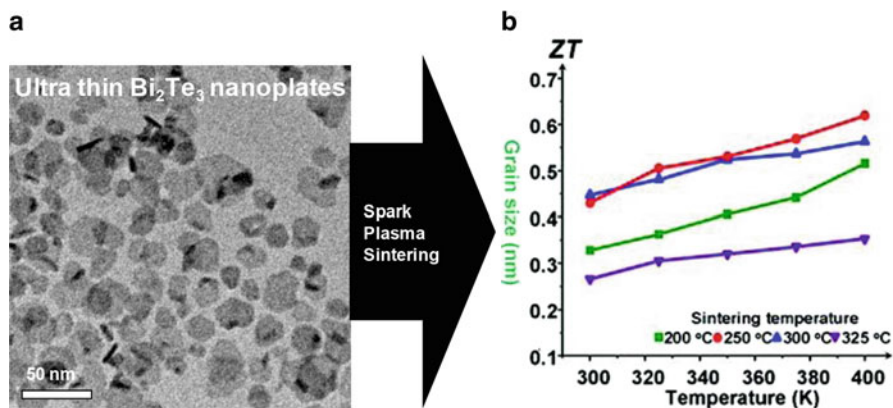
Fig. 8.4 Large-scale synthesis of ultrathin Bi_2Te_3 nanoplates and subsequent spark plasma sintering to fabricate *n*-type nanostructured bulk thermoelectric materials. (**a**) The transmission electron microscopy (TEM) image of as-synthesized ultrathin Bi_2Te_3 nanoplates. (**b**) Temperature dependence of *ZT (zT)* of nanostructured bulk Bi_2Te_3 sintered at 200 °C (green square), 250 °C (red circle), 300 °C (blue upward triangle) and 325 °C (purple downward triangle). Adapted with permission from Ref. [31] © 2012, American Chemical Society

Son et al. have reported TE properties of SPS-processed ultrathin (1–3 nm) *n*-type Bi_2Te_3 nanoplates (Fig. 8.4) [31]. Bi_2Te_3 nanoplates have been synthesized by the reaction between bismuth dodecanethiolate and tri-n-octylphosphine telluride in the presence of oleylamine. The highest *zT* of 0.62 has been achieved in the SPS-processed sample sintered at 250 °C, which is one of the highest values among those reported for *n*-type chemically synthesized nanosheets (Fig. 8.4).

8.4.2   Bismuth Selenide

Bismuth selenide (Bi_2Se_3), another narrow band gap semiconductor ($\sim$0.3 eV), has potential application in the field of thermoelectrics [36–39]. Like Bi_2Te_3, it is also a 3D topological insulator (TI), where metallic surface states are protected by the time-reversal symmetry [22]. Bi_2Se_3 is a layered anisotropic material (space group: R-3 m) accommodating quintuple layers (QL) each of which are having thickness of $\sim$1 nm and composed of five covalently bonded atomic planes [Se2–Bi–Se1–Bi–Se2]. Thus, synthesis of atomically thin Bi_2Se_3 nanosheets is desirable for TE application. Sun et al. synthesized single layered Bi_2Se_3 via a scalable intercalation/exfoliation strategy, by using Li-intercalated Bi_2Se_3 microplates as an intermediate precursor [22]. Bi_2Se_3 nanosheets sample shows high carrier mobility (μ) of $\sim$6000 cm^2 V^{-1} s^{-1} which can be attributed to the 2D electron gas like nature [22, 62]. The single-layer-based (SLB) Bi_2Se_3 composite has shown a huge improvement in electric transport properties and ultralow thermal conductivity than

that of the bulk counterpart over the entire temperature range. Thus, the σ/κ_{total} ratio for the SLB composite is superior to that of the bulk material over the whole temperature range. $|S|$ for the SLB composite gradually increases from 90 μV/K at 300 K to 121 μV/K at 400 K, which is greater than that of bulk material ($\sim$98.5 μV/K at 400 K). Thus, zT for the SLB composite is higher than that for the bulk material over the entire temperature range. Specifically, the SLB composite exhibits zT of 0.35 at 400 K, which is eight times larger than zT of the bulk Bi_2Se_3 and higher than the previously reported values for pure Bi_2Se_3 nanostructures, suggesting the advantage of the atomically thick SLB structure over bulk one (Fig. 8.5).

Jana et al. have investigated the TE properties of few-layer Bi_2Se_3 nanosheets, synthesized via a green ionothermal reaction in the water-soluble, room-temperature ionic liquid, 1-ethyl-3-methylimidazolium tetrafluoroborate ([EMIM][BF$_4$]) [62]. Ionothermal reaction of bismuth acetate and selenourea in [EMIM][BF$_4$] results in ultrathin few-layer (3–5 layer) Bi_2Se_3 nanosheets. The high σ of Bi_2Se_3 nanosheets originates from the presence of metallic surface states that offer high mobility and
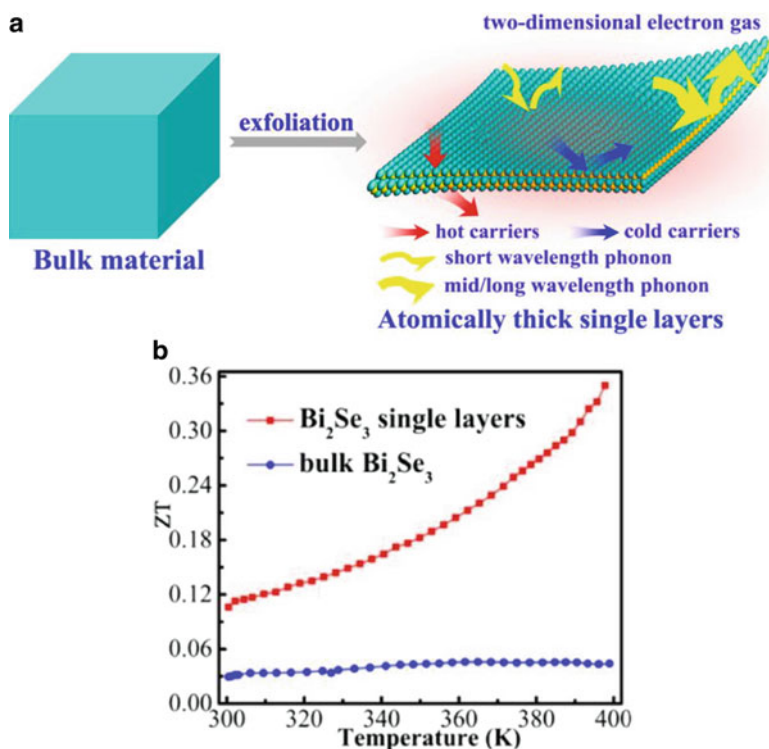

Fig. 8.5 (**a**) Schematic representation of exfoliation technique and electronic and phonon transport in single layer Bi_2Se_3. (**b**) Temperature dependent ZT (zT) of bulk and single layered Bi_2Se_3. Adapted with permission from Ref. [22] © 2012, American Chemical Society

scattering resistant carriers transport. In addition to this, surface defects, nanoscale grain boundaries and interfaces effectively scatter the heat carrying phonons, thereby decreasing κ_{total} to ~0.4 Wm^{-1} K^{-1} near room temperature.

8.4.3 Antimony Telluride

Antimony telluride (Sb_2Te_3) is a narrow-band gap (~0.28 eV) layered semiconductor with tetradymite structure [63]. Single-crystalline Sb_2Te_3 nanosheets with lateral dimension of 300–500 nm and thicknesses of 50–70 nm were rapidly synthesized by a microwave-assisted reaction of $SbCl_3$, Na_2TeO_3 and $N_2H_4.5H_2O$ in ethylene glycol at 200 °C [64]. For thermoelectric measurements, nanostructured bulk Sb_2Te_3 was prepared from Sb_2Te_3 nanosheets via SPS. High electrical conductivity (~2.49 × 10^4 Sm^{-1}), high Seebeck coefficient (~210 μVK^{-1}) and low thermal conductivity (~0.76 Wm^{-1} K^{-1}) at 420 K were achieved, which resulted in zT of 0.58 at 420 K for the Sb_2Te_3 nanosheets sample.

Dong et al. have explored rapid microwave-assisted solvothermal synthesis and thermoelectric properties of Sb_2Te_3 nanosheets [65]. Antimony trichloride anhydrous ($SbCl_3$), tellurium dioxide (TeO_2), polyethylene glycol (PEG) and hydrazine hydrate ($N_2H_4.5H_2O$) were used to synthesize the nanostructured Sb_2Te_3 in the presence of ethylene glycol (EG) as a solvent. The thermoelectric properties of the Sb_2Te_3 pellet obtained by room-temperature pressing of powdered nanosheets were studied at the temperatures ranging from 300 to 450 K. Sb_2Te_3 nanosheets samples show the characteristics of p-type semiconductors. Sb_2Te_3 nanosheets exhibit Seebeck coefficient of ~194–245 μVK^{-1} and power factor of 0.48–1.14 × 10^{-4} Wm^{-1} K^{-2} in the temperature range of 300–450 K.

8.4.4 Solid Solutions and Nanocomposites of Bi₂Te₃ and Bi₂Se₃

Solid solutions and nanocomposites of Bi_2Te_3, Bi_2Se_3 and Sb_2Te_3 nanosheets have been explored for thermoelectric application. Because of the isomorphic crystal structure of Bi_2Te_3 and Bi_2Se_3, the solubility of Se in Bi_2Te_3 results in a modification of the crystal lattice and electronic density of states (DOS), which is beneficial for reduction of the bipolar conduction and is an important factor for the advancement of thermoelectric properties of Bi_2Te_3 alloys. Min et al. have presented TE properties of $Bi_2Te_{3-x}Se_x$ nanocomposite pellets [66]. Figure 8.6 presents TE properties of the as-prepared pellets by mixing appropriate ratios of the Bi_2Te_3 and Bi_2Se_3 nanoflakes. The electrical conductivities (σ) of the nanocomposites systematically increased in the range of 200–440 Scm^{-1} at room temperature as the Bi_2Se_3 amount has been enhanced (Fig. 8.6a). The Seebeck coefficient is negative
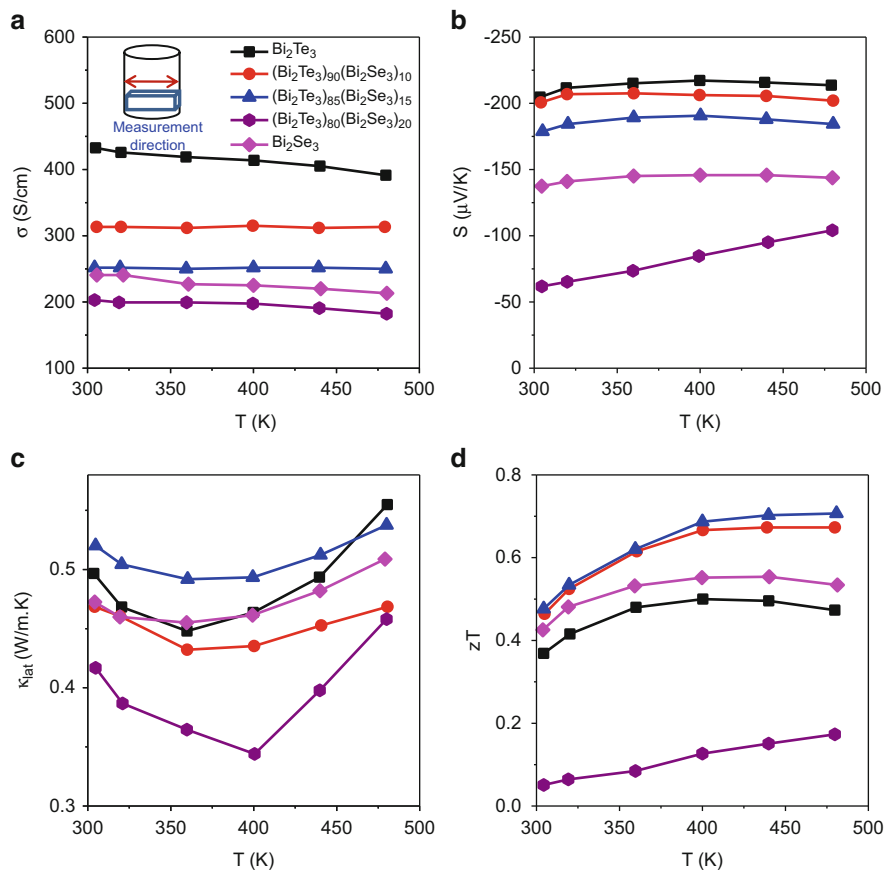
Fig. 8.6 Temperature dependent (**a**) electrical conductivities (σ), (**b**) Seebeck coefficients (S), (**c**) lattice thermal conductivities (κ_{lat}) and (**d**) thermoelectric figure of merit (zT) for nanocomposite of Bi_2Te_3 and Bi_2Se_3. Inset in (**a**) shows schematic of sintered pellet along with thermoelectric measurement directions. Adapted with permission from Ref. [66] © 2013, John Wiley and Sons

(Fig. 8.6b) indicating electrons as the major charge carriers. The absolute value of S increased as the measurement temperature has been raised to 360 K. S has increased with the increasing composition of the Bi_2Se_3 nanoflakes. The maximum value of S was found for $(Bi_2Te_3)_{85}(Bi_2Se_3)_{15}$ which can be attributed to the carrier energy filtering effect originating from the presence of Bi_2Se_3 nanoflakes in the Bi_2Te_3 matrix. The maximum power factor (1.2 mW m^{-1} K^{-2} at 400 K) in this study was obtained in $(Bi_2Te_3)_{85}(Bi_2Se_3)_{15}$. The κ_{total} values of the nanocomposites ranged from 0.55 to 0.68 Wm^{-1} K^{-1} at room temperature, which is significantly lower than that of the bulk Bi_2Te_3 with micro-sized grains ($\sim$1.5 Wm^{-1} K^{-1}). This reduction of κ_{total} is attributed to the reduction of κ_{lat} due to the phonon scattering at the interfaces of the randomly oriented nanograins (5–20 nm). Room temperature

κ_{lat} values of the nanocomposites decreased by about 40% (0.43–0.52 Wm^{-1} K^{-1}) (Fig. 8.6c). The reduced κ_{total} and the enhanced power factor result in maximum thermoelectric figure of merit (zT) of ~0.71 at 480 K for $(Bi_2Te_3)_{90}(Bi_2Se_3)_{10}$ samples (Fig. 8.6d).

8.4.5   SnSe

SnSe, an environment-friendly layered chalcogenide, has drawn enormous consideration of the TE community with their high thermoelectric performance in single crystals [67–69]. SnSe crystallizes in layered orthorhombic crystal structure (space group *Pnma*, lattice parameters, $a = 11.502$ Å, $b = 4.15$ Å, $c = 4.45$ Å) at room temperature with sterically accommodated lone pair [69]. When temperature increases (~800 K), SnSe undergoes a second-order displacive phase transition to a higher symmetric five-fold coordinated *Cmcm* phase [69]. The two-atom-thick SnSe slabs are folded up and create a zigzag accordion-like projection along the crystallographic *b* axis. In both the structures these identical layers are weakly bound via weak van der Waals interaction and resulting in an anisotropic layered structure. Han et al. have recently developed a surfactant-free simple solution-based technique, using water as a solvent, for the synthesis of phase pure gram scale orthorhombic SnSe nanoplates [70]. Hot-pressed SnSe nanosheets exhibit outstanding electrical conductivity (σ) and power factors (σS^2). Recently, Chandra et al. have reported the solution phase synthesis and thermoelectric transport properties of two-dimensional (2D) ultrathin few-layer nanosheets (2–4 layers) of *n*-type SnSe using $SnCl_4 \cdot 5H_2O$ and SeO_2 as a preliminary precursor [71]. The *n*-type nature of the SnSe nanosheets arises from in situ chlorination during the synthesis. The carrier concentration of *n*-type SnSe has been significantly increased from 3.08×10^{17} cm^{-3} to 1.97×10^{18} cm^{-3} via Bi-doping which results in the significant rise of electrical conductivity and power factor (Fig. 8.7). Typically, $Sn_{0.94}Bi_{0.06}Se$ nanosheets ($\perp$ to pressing direction) have S value of -219 μV/K at 300 K, which increases to -285 μV/K at 719 K. Furthermore, Bi-doped nanosheets exhibit ultralow lattice thermal conductivity (~0.3 W/mK) throughout the temperature range of 300–720 K originating from the effective phonon scattering by interface of SnSe layers, nanoscale grain boundaries and point defects.

8.4.6   SnSe$_2$

Tin diselenide (SnSe$_2$) is an additional layered compound from the phase diagram of Sn-Se [72–74]. Our group has reported the synthesis of *n*-type ultrathin few-layer SnSe$_2$ nanosheets via the simple solution-based low temperature synthesis, which exhibits semiconducting electronic transport (Fig. 8.8) [72]. An ultralow
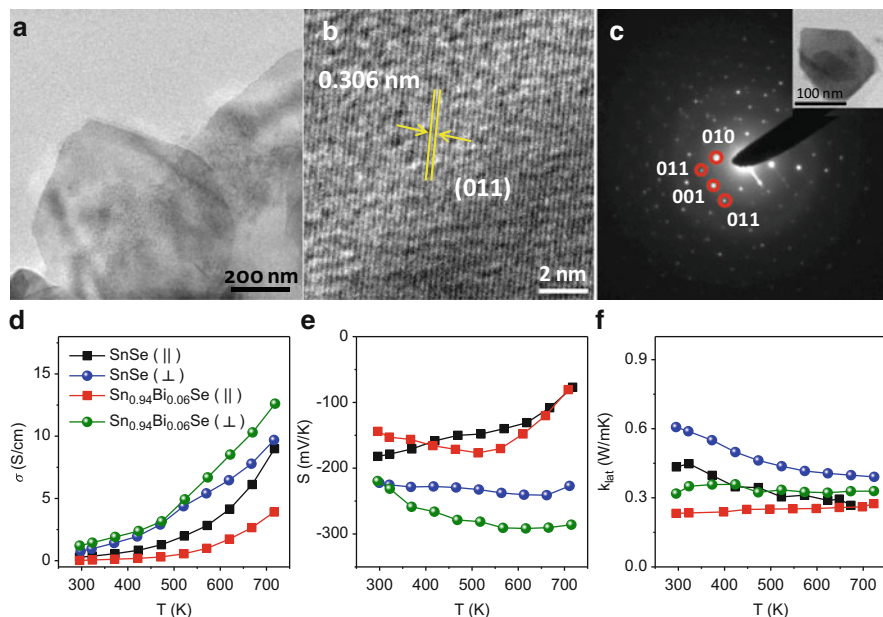
Fig. 8.7 (**a**) TEM image of $Sn_{0.94}Bi_{0.06}Se$ nanosheets. (**b**) HRTEM image of $Sn_{0.94}Bi_{0.06}Se$ nanosheets. (**c**) SAED pattern of a single $Sn_{0.94}Bi_{0.06}Se$ nanosheet. Inset of (**c**) shows the STEM image of single nanosheet of $Sn_{0.94}Bi_{0.06}Se$. Temperature dependent (**d**) electrical conductivity (σ), (**e**) Seebeck coefficient, (*S*) and (**f**) lattice thermal conductivity (κ_{lat}) of SnSe and $Sn_{0.94}Bi_{0.06}Se$ nanosheets measured along the SPS direction (indicated by squares) and perpendicular to the SPS direction (indicated by spheres). Adapted with permission from Ref. [71] © 2018, American Chemical Society

thermal conductivity ($\sim$0.67 Wm^{-1} K^{-1}) has been achieved due to the anisotropic layered structure, which results in effective phonon scattering at layered interface and grain boundaries. However, the low carrier concentration ($\approx$10^{18} cm^{-3}) and randomly oriented grains still result in a low power factor ($\approx$150 μWm^{-1} K^{-2}). Thermoelectric properties of SnSe$_2$ have been improved by Kanatzidis and co-worker by simultaneously introducing a selenium (Se) deficiency and chlorine (Cl) doping in SnSe$_2$ nanoplate-based pellets, in which the nanoplates show a preferred orientation of the (001) planes along the primary surface of the pellet (in-plane) [73]. This yields a sharp increase in the in-plane electrical conductivity and power factor. The SnSe$_2$ nanoplate-based pellets have been prepared via a two-step process: (1) the synthesis of precursor bulk ingots by a vacuum-sealed high temperature melting process, followed by ball-milling grinding of the ingots; (2) obtaining the nanoplate-based pellets through the densification of ground precursors in SPS process. The electrical resistivity (ρ) of the Se-deficient and halogen-doped samples is much lower than that of the pristine SnSe$_2$ over the entire temperature range (Fig. 8.9). As a result, an improved in-plane thermoelectric figure of merit, $zT_{max,}$ of 0.63 is
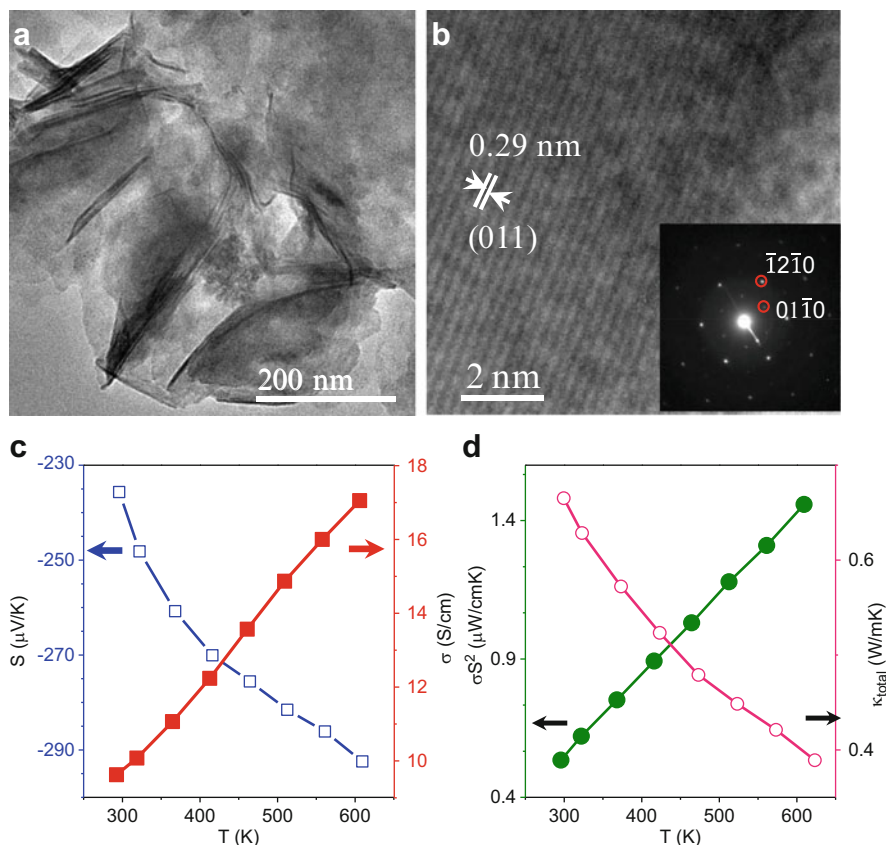
Fig. 8.8 (**a**) TEM image of Cl-doped SnSe$_2$ nanosheets. (**b**) HRTEM image of Cl-doped SnSe$_2$ nanosheets showing distance between (011) planes. Inset of (**b**) shows SAED pattern of a single nanosheet. Temperature dependent (**c**) Seebeck coefficient (S) and electrical conductivity (σ), and (**d**) power factor (σS^2) and thermal conductivity (κ_{total}) of SnSe$_2$ nanosheets. Adapted with permission from Ref. [72] © 2016, John Wiley and Sons

obtained for a 1.5 at% Cl-doped SnSe$_{1.95}$ pellet at 673 K, which is significantly higher than the corresponding in-plane zT of pure SnSe$_2$ (0.08) (Fig. 8.9).

8.4.7 Layered Intergrowth Chalcogenides

Layered intergrowth inorganic compounds in the homologous series have drawn the attention of thermoelectric community due to their ultralow thermal conductivity [75–79]. Phase homology is a collective demonstration of various structures built on the same structural principle with a certain module(s) expanding in different

Fig. 8.9 Temperature dependent (**a**) electrical resistivity (ρ) and (**b**) ZT (zT) of the 1.5 at% Cl doped SnSe$_{1.95}$ sample and p-type polycrystalline SnSe sample measured along in-plane and cross-plane direction. Adapted with permission from Ref. [73] © 2017, John Wiley and Sons
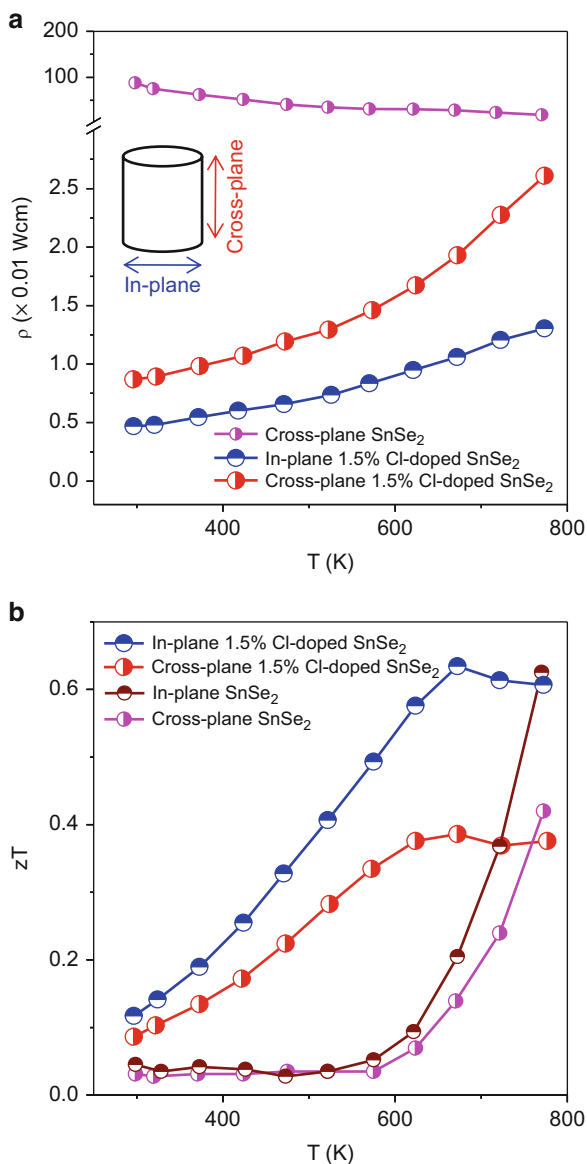
dimensions in standard increments. The modules are usually infinite rods, cluster blocks or layers, which can be consolidated in various ways to frame each member via coordination chemistry principles or structure building operators, reflection twinning, glide reflection twinning, cyclic twinning, unit cell intergrowth, etc. [75] The homologous series is represented by a mathematical formula which is able to produce each member [75, 80]. In solid-state inorganic chemistry, the use of

phase homologies is a well-established approach to predict new compounds with a predictable structure. The general representation of some of the series includes $A_m(M'_{1+l}Se_{2+l})_{2m}(M''_{2l+n}Se_{2+3l+n})$ (A = alkali metal; M', M'' = main group element), $Cs_4(Bi_{2n+4}Te_{3n+6})$ and $(Sb_2Te_3)_m(Sb_2)_n$ [75, 80, 81]. These materials are structurally as well as electronically anisotropic in nature, which can have a positive impact on the thermoelectric properties.

Layered intergrowth compounds from the homologous series of quasi-binary $(A^{IV}B^{VI})_m(A^V_2B^{VI}_3)_n$ systems, where A^{IV} = Ge, Sn, Pb; A^V = Sb, Bi and B^{VI} = Se, Te, are predicted to show promising thermoelectric performance [75, 82]. These compounds crystallize in anisotropic layered tetradymite Bi_2Te_2S-type structures [82–86]. Most of the layered compounds in the above homologous series resemble natural van der Waals heterostructure and are anticipated to be 3D-topological insulators [87–90]. These compounds are predicted to show low κ_{lat} due to complex crystal structure and strong phonon scattering at the interfaces between the layers [82, 84]. However, it is really difficult to synthesize these compounds in pure phases through high temperature solid-state melting technique due to their incongruent melting nature (Fig. 8.10a) [83, 84]. Preparation of these compounds in nanosheets form can provide excess metallic surfaces with scattering resistant transport and high carrier mobility. Potential applications of these intergrowth nanosheets in the field of topological materials and thermoelectrics have grown interest to study the layered complex compounds in the pseudo-binary homologous series. As an example, we can consider $(SnTe)_m$-$(Bi_2Te_3)_n$ series, where $SnBi_2Te_4$, $SnBi_4Te_7$ and $SnBi_6Te_{10}$ are distinguished members (Fig. 8.10) [84]. They can also be visualized as intergrowths of SnTe-type rocksalt and Bi_2Te_3-type hexagonal phases, which are indeed natural heterostructures [84]. In the unit cell of $SnBi_2Te_4$ (rhombohedral structure, R-3m space group), septuple layers are stacked along the c-axis by van der Waals interactions. Each septuple layer is composed of seven covalently bonded atomic planes [Te2–Bi–Te1–Sn–Te1–Bi–Te2] with 1.13 nm thickness (Fig. 8.10b). Layered intergrowth compound, $SnBi_4Te_7$ [i.e. $(SnTe)_1(Bi_2Te_3)_2$] crystallizes in trigonal structure (P-3m1 space group) with a long unit cell (c = 2.406 nm). The $SnBi_4Te_7$ crystal structure contains two subunits, a quintuple layered (QL) Bi_2Te_3 and a septuple layered (SL) $SnBi_2Te_4$, assembled along the c-axis with the 5757 sequences by van der Waals interactions (Fig. 8.10c). In $SnBi_6Te_{10}$ [i.e. $(SnTe)_1(Bi_2Te_3)_3$], $SnBi_2Te_4$ and Bi_2Te_3 subunits are assembled along the c-axis in 7557 sequence (Fig. 8.10d). Similarly, several layered intergrowth compounds exist in the $(PbTe)_m$-$(Bi_2Te_3)_n$ and $(PbTe)_m$-$(Bi_2Se_3)_n$. Recently, 2D ultrathin nanosheets of various layered compounds from homologous $A_mBi_{2n}Te_{3n+m}$ have been synthesized by low temperature solution-based bottom up method and their thermoelectric properties have been investigated [83, 84]. The nanosheets were characterized using various experimental techniques (Fig. 8.11). Atomic force microscopy (AFM) and transmission electron microscopy (TEM) measurement indicate the ultrathin nature of the nanosheets. HAADF-STEM imaging confirms van der Waals heterostructured nature of nanosheets. Few-layer nanosheets indeed exhibit semiconducting electronic-transport properties with high carrier mobility (Fig. 8.12a, b). Long periodic intergrowth structure and effective phonon scattering
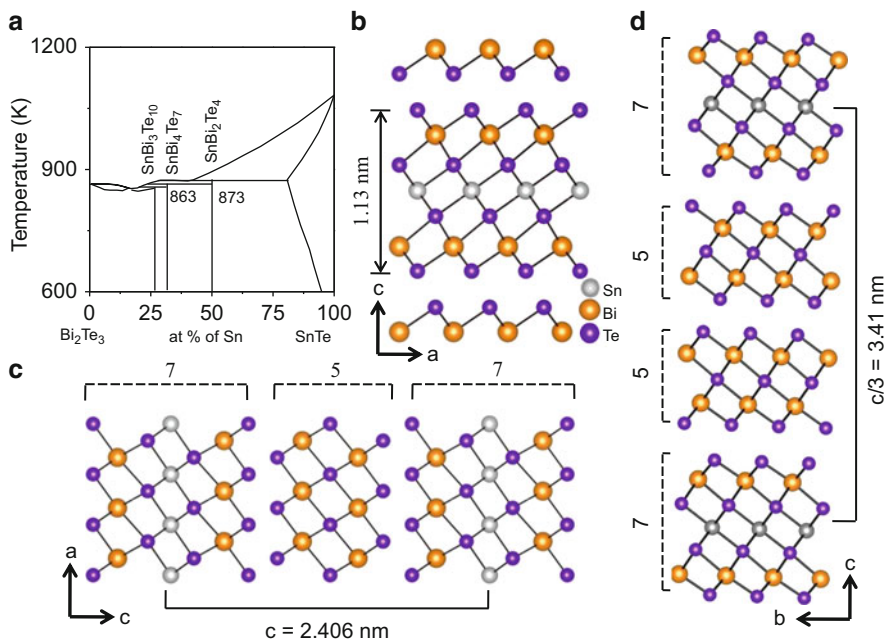
Fig. 8.10 (**a**) Existence of incongruently melting layered ternary intergrowth tin chalcogenide compounds in the SnTe–Bi$_2$Te$_3$ pseudo-binary phase diagram. (**b**) Crystal structure of SnBi$_2$Te$_4$ showing the 1.13 nm thick septuple atomic layers. (**c**, **d**) Crystal structure of natural van der Waals heterostructure SnBi$_4$Te$_7$ and SnBi$_6$Te$_{10}$ showing different stacking sequences of quintuple layers of Bi$_2$Te$_3$ and septuple layers of SnBi$_2$Te$_4$

at the interface lead to low thermal conductivity (κ_{lat} of 0.3–0.5 Wm^{-1} K^{-1}) for these 2D nanosheets (Fig. 8.12c).

8.4.8 BiCuSeO

Layered quaternary metal oxychalcogenide, MCuXO (M = La, Ce, Nd, Pr, Bi and In; X = Te, Se and S) is reported to show superior properties in various fields like thermoelectrics and superconductivity [91, 92]. BiCuSeO, a multiband semiconductor and a promising TE material from this oxychalcogenide family [93]. It crystallizes in ZrCuSiAs-type layered structure with a tetragonal unit cell (space group P4/nmm). BiCuSeO crystal structure comprises of insulating (Bi$_2$O$_2$)$^{2+}$ and conducting (Cu$_2$Se$_2$)$^{2-}$ layers, which are stacked along the crystallographic c-axis of the tetragonal cell (Fig. 8.13a) [93]. The (Bi$_2$O$_2$)$^{2+}$ layers are composed by distorted Bi$_4$O tetrahedra (fluorite type structure), whereas (Cu$_2$Se$_2$)$^{2-}$ layers contain distorted CuSe$_4$ tetrahedra (anti-fluorite type structure). The ultralow κ_{lat} originates from the scattering of phonons from the interface due to the layered structure, soft

Fig. 8.11 (**a**) AFM image of a SnBi$_2$Te$_4$ nanosheet. The inset in (**a**) shows the Tyndall light scattering effect of SnBi$_2$Te$_4$ nanosheet dispersed in toluene. (**b**) TEM image of a SnBi$_2$Te$_4$ nanosheet. The inset in (**b**) shows the SAED pattern of a single SnBi$_2$Te$_4$ nanosheet. (**c**) HRTEM image showing the crystalline nature of as-synthesized of SnBi$_2$Te$_4$ nanosheet. (**d**) HAADF-STEM image shows long-range ordered sequence of SnBi$_2$Te$_4$ blocks with a schematic of the atomic layer sequence in structures built from SnBi$_2$Te$_4$. (**e**) AFM image of a SnBi$_4$Te$_7$ nanosheet. (**f**) TEM image of SnBi$_4$Te$_7$ nanosheet. The inset in (**f**) shows the SAED pattern of a single SnBi$_4$Te$_7$ nanosheet. (**g**) HRTEM image of a SnBi$_4$Te$_7$ nanosheet. (**h**) HAADF-STEM image of SnBi$_4$Te$_7$ showing presence of 57 stacking of Bi$_2$Te$_3$ and SnBi$_2$Te$_4$. Adapted with permission from Ref. [84] © 2017, John Wiley and Sons
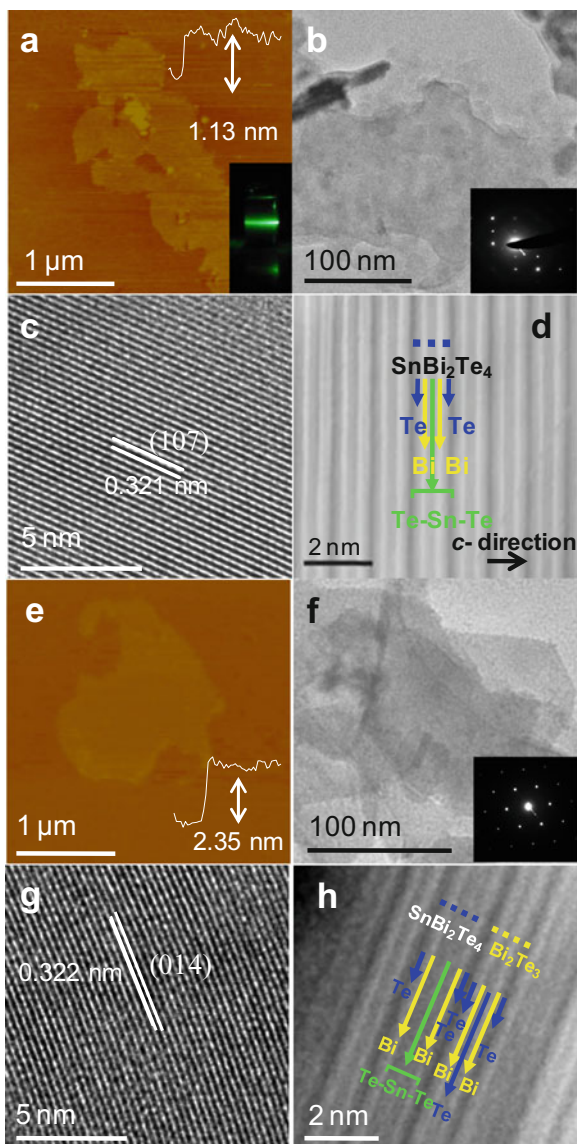
bonding and lattice anharmonicity, which result in low κ_{lat} in BiCuSeO. A recent study by Samanta et al. has explored the synthesis of few-layered ultrathin BiCuSeO nanosheets via a facile surfactant-free low temperature solvothermal synthesis [94]. Large-scale few-layered BiCuSeO nanosheets (Fig. 8.13b–d) have been synthesized by the reaction of Bi(NO$_3$)$_2$·5H$_2$O, Cu(NO$_3$)$_2$·3H$_2$O and selenourea in the presence of KOH/NaOH under solvothermal conditions. BiCuSeO nanosheets exhibit lower lattice thermal conductivity (0.55–0.4 Wm^{-1} K^{-1}) compared to that of the bulk

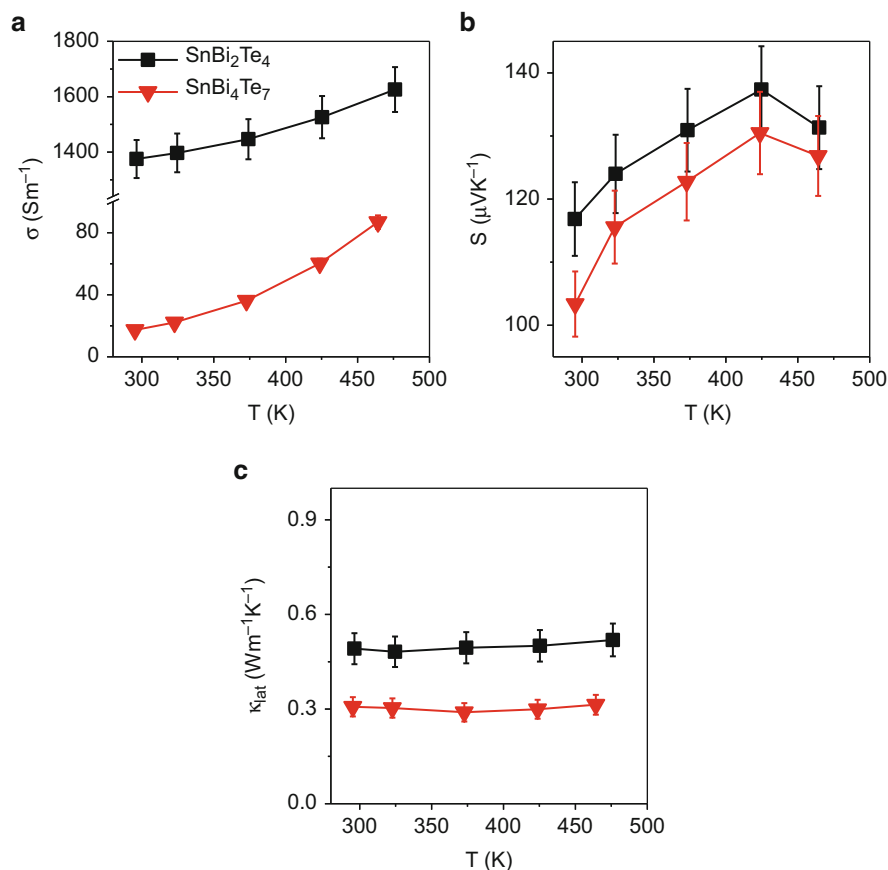**Fig. 8.12** Temperature-dependent (**a**) electrical conductivity (σ), (**b**) Seebeck coefficient (S) and (**c**) lattice thermal conductivity (κ_{lat}) of $SnBi_2Te_4$ and $SnBi_4Te_7$ nanosheets with 5% error bar. Adapted with permission from Ref. [84] © 2017, John Wiley and Sons

sample (Fig. 8.13f). Significant phonon scattering from the interfaces of the layers, bond anharmonicity and nanoscale grain boundaries resulted in low thermal conductivity in BiCuSeO nanosheets. Thus, nanosheets of pristine BiCuSeO demonstrate potential application in thermoelectric energy harvesting.

8.4.9 Cu₂Se

As one of the promising thermoelectric materials, Cu_2Se provides opportunities to overcome the global energy crisis via the conversion of waste heat into electricity [95]. Low temperature α-Cu_2Se phase has a complex monoclinic crystal structure
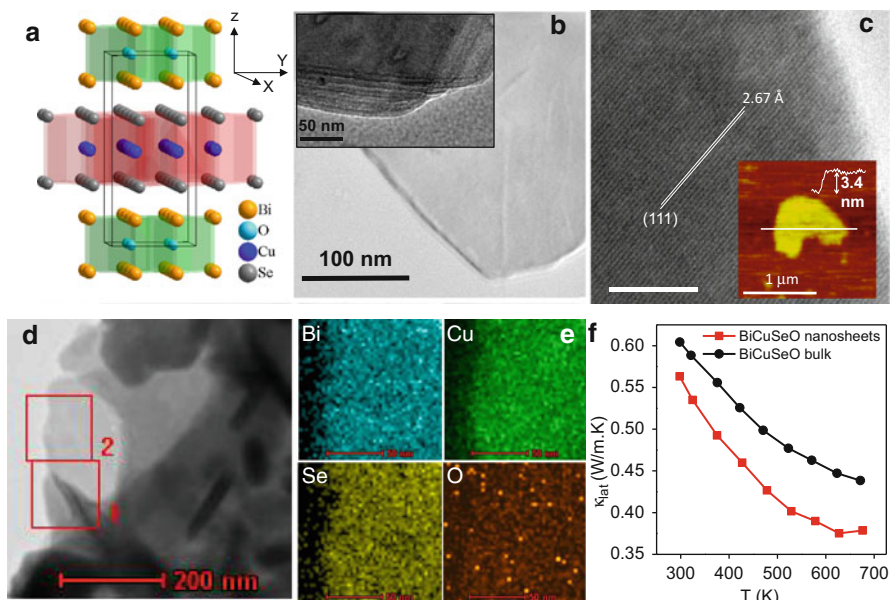
Fig. 8.13 (**a**) Crystal structure of BiCuSeO demonstrating the layered structure. (**b**) Ultrathin van der Waals heterostructured nanosheets of layered quaternary metal oxychalcogenide, BiCuSeO. Inset image shows that the bent edges of several BiCuSeO nanosheets are stacked one over another. (**c**) HRTEM image of the BiCuSeO nanosheets showing the crystalline nature and lattice spacing between (111) planes. The inset image demonstrates an AFM image of the BiCuSeO nanosheets and the height profile showing a thickness of ~3.4 nm. (**d**) STEM image of the BiCuSeO nanosheets. (**e**) EDAX colour mapping for Bi, Cu, Se and O in the BiCuSeO nanosheets during STEM imaging (from the highlighted portion (numbered as 2) of the STEM image). (**f**) Temperature dependent lattice thermal conductivity (κ_{lat}) of BiCuSeO nanosheets (marked in red) and bulk BiCuSeO (marked in black). Adapted with permission from Ref. [94] © 2017, Royal Society of Chemistry

with 144 atoms per unit cell. When the temperature increases to 400 K, α-Cu_2Se transforms to a high temperature β-phase with Fm-3m space group. During the phase transition, Cu^+ ions assemble in the ordered stack along the <111> directions to form a simple anti-fluorite structure. Such a phase transformation is reversible through cooling or heating processes. In case of β-Cu_2Se crystal structure, Se atoms form a face-centred-cubic (FCC) frame and Cu^+ ions behave like liquid (high mobility) with a reduced phonon mean free path [96], which results in a low κ_{lat} value of 0.4–0.6 Wm^{-1} K^{-1}. Yang et al. have studied thermoelectric properties of SPS-processed β-phase Cu_2Se nanoplates [95]. Significantly enhanced phonon scattering achieved by high-density small-angle grain boundaries and dislocations efficiently block phonons with long and intermediate mean free paths. Moreover, Cu^+ ions strongly scatter phonons with a short mean free path. This full-spectrum phonon scattering has a negligible control over the electrical transport because electrons are having very short mean free path which can transport through grains.
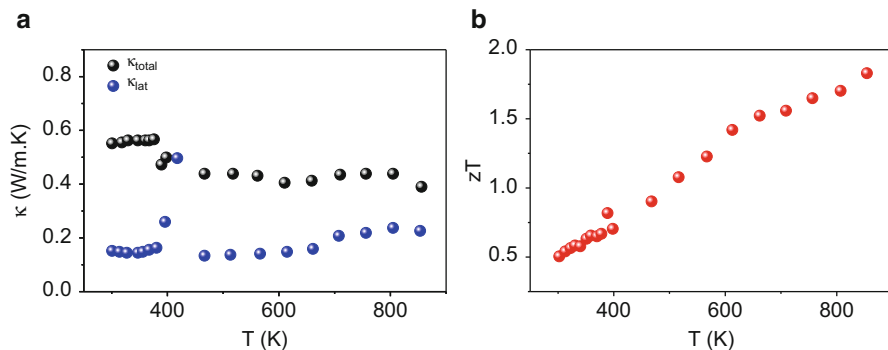
Fig. 8.14 Temperature dependent (**a**) thermal conductivities and (**b**) zT of Cu$_2$Se. Adapted with permission from Ref. [95] © 2015, Elsevier

Thus, an ultra-low κ_{lat} ($\sim$0.2 Wm^{-1} K^{-1}) and zT of 1.82 has been achieved in SPS-processed Cu$_2$Se pellets (Fig. 8.14). Such an enhanced zT could be attributed to its very low κ_{lat}, which benefits from the strong phonon scattering by high densities of small-angle grain boundaries and dislocations within the boundaries via nanostructure engineering.

8.5 Conclusions and Future Directions

In this chapter, we have discussed the key concepts, latest development and under-standing of the thermoelectric properties of metal chalcogenides nanosheets and 2D thin films prepared by physical and chemical routes. However, thermoelectric thin film metrology is yet to be reinvestigated as uncertainty in thin film measurement is still a challenging task, especially measurement of cross-plane TE properties of 2D materials. Nevertheless, Bi$_2$Te$_3$-based nanosheets and thin films are still considered as leading thermoelectric materials for near room temperature power generation and refrigeration applications, while SnSe, Cu$_2$Se nanosheets are observed to be potential candidates for the mid-to-high temperature power generation.

Generally, layered metal chalcogenides show intrinsically low thermal conductivity due to anisotropic structure and strong lattice anharmonicity. Intergrowth homologous chalcogenides are new candidates for thermoelectric applications as they exhibit low thermal conductivity due to long periodic intergrowth structure. The studies on the thermoelectric properties of layered chalcogenides are vibrant and open area of research. Although the thermal conductivity is intrinsically low for layered chalcogenides, attention should be given on improving the Seebeck coefficient by various innovative approaches such as electronic band valley conver-gence and exploration of resonance level in the electron structure. Many new layered materials with promising thermoelectric properties have been discovered, although

a lot of work and progress need to be done for their practical realization in the form of thermoelectric module. In this context, the combined effort from chemistry, physics, materials scientists and engineers will certainly lead to the achievement of high performance 2D chalcogenide-based TE materials and fabrication of highly efficient TE devices for localized power generation, small-scale electronic systems and for booting-up the conventional combustion gasoline heat engines.

References

1. G. Tan, L.-D. Zhao, M.G. Kanatzidis, Chem. Rev. **116**(19), 12123 (2016)
2. C. Xiao, Z. Li, K. Li, P. Huang, Y. Xie, Acc. Chem. Res. **47**(4), 1287 (2014)
3. J. He, T.M. Tritt, Science **357**(6358), eaak9997 (2017)
4. R. Venkatasubramanian, E. Siivola, T. Colpitts, B. O'Quinn, Nature **413**(6856), 597 (2001)
5. Y. Zhou, L.-D. Zhao, Adv. Mater. **29**(45), 1702676 (2017)
6. Y. Pei, X. Shi, A. LaLonde, H. Wang, L. Chen, G.J. Snyder, Nature **473**(7345), 66 (2011)
7. A. Banik, U.S. Shenoy, S. Anand, U.V. Waghmare, K. Biswas, Chem. Mater. **27**(2), 581 (2015)
8. S.V. Faleev, F. Léonard, Phys. Rev. B **77**(21), 214304 (2008)
9. L.D. Hicks, M.S. Dresselhaus, Phys. Rev. B **47**(19), 12727 (1993)
10. L.D. Hicks, T.C. Harman, X. Sun, M.S. Dresselhaus, Phys. Rev. B **53**(16), R10493 (1996)
11. M.S. Dresselhaus, G. Dresselhaus, X. Sun, Z. Zhang, S.B. Cronin, T. Koga, Phys. Solid State **41**(5), 679 (1999)
12. J.P. Heremans, V. Jovovic, E.S. Toberer, A. Saramat, K. Kurosaki, A. Charoenphakdee, S. Yamanaka, G.J. Snyder, Science **321**(5888), 554 (2008)
13. P.G. Klemens, Phys. Rev. **119**(2), 507 (1960)
14. M. Samanta, K. Biswas, J. Am. Chem. Soc. **139**(27), 9382 (2017)
15. K. Biswas, J. He, Q. Zhang, G. Wang, C. Uher, V.P. Dravid, M.G. Kanatzidis, Nat. Chem. **3**(2), 160 (2011)
16. K.F. Hsu, S. Loo, F. Guo, W. Chen, J.S. Dyck, C. Uher, T. Hogan, E.K. Polychroniadis, M.G. Kanatzidis, Science **303**(5659), 818 (2004)
17. K. Biswas, J. He, I.D. Blum, C.-I. Wu, T.P. Hogan, D.N. Seidman, V.P. Dravid, M.G. Kanatzidis, Nature **489**(7416), 414 (2012)
18. D.T. Morelli, V. Jovovic, J.P. Heremans, Phys. Rev. Lett. **101**(3), 035901 (2008)
19. S.N. Guin, A. Chatterjee, D.S. Negi, R. Datta, K. Biswas, Energy Environ. Sci. **6**(9), 2603 (2013)
20. G. Tan, F. Shi, S. Hao, L.-D. Zhao, H. Chi, X. Zhang, C. Uher, C. Wolverton, V.P. Dravid, M.G. Kanatzidis, Nat. Commun. **7**, 12167 (2016)
21. S.N. Guin, A. Banik, K. Biswas, Thermoelectric energy conversion in layered metal Chalcogenides, in *2d Inorganic Materials Beyond Graphene*, (World Scientific (WS), London, 2017), p. 239
22. Y. Sun, H. Cheng, S. Gao, Q. Liu, Z. Sun, C. Xiao, C. Wu, S. Wei, Y. Xie, J. Am. Chem. Soc. **134**(50), 20294 (2012)
23. T.C. Harman, P.J. Taylor, M.P. Walsh, B.E. LaForge, Science **297**(5590), 2229 (2002)
24. H. Böttner, G. Chen, R. Venkatasubramanian, MRS Bull. **31**(3), 211 (2006)
25. L.D. Hicks, M.S. Dresselhaus, Phys. Rev. B **47**(24), 16631 (1993)
26. D.A. Broido, T.L. Reinecke, Phys. Rev. B **51**(19), 13797 (1995)
27. B. Poudel, Q. Hao, Y. Ma, Y. Lan, A. Minnich, B. Yu, X. Yan, D. Wang, A. Muto, D. Vashaee, X. Chen, J. Liu, M.S. Dresselhaus, G. Chen, Z. Ren, Science **320**(5876), 634 (2008)

28. N.F. Mott, H. Jones, *The Theory of the Properties of Metals and Alloys* (Dover Publications, New York, 1958)
29. D.M. Rowe, *CRC Handbook of Thermoelectrics* (CRC press, Boca Raton, 1995)
30. J.P. Heremans, B. Wiendlocha, A.M. Chamoire, Energy Environ. Sci. **5**(2), 5510 (2012)
31. J.S. Son, M.K. Choi, M.-K. Han, K. Park, J.-Y. Kim, S.J. Lim, M. Oh, Y. Kuk, C. Park, S.-J. Kim, T. Hyeon, Nano Lett. **12**(2), 640 (2012)
32. G. Chen, J. Heat Transf. **119**(2), 220 (1997)
33. H.J. Goldsmid, R.W. Douglas, Br. J. Appl. Phys. **5**(12), 458 (1954)
34. M. Takashiri, S. Tanaka, K. Miyazaki, Thin Solid Films **519**(2), 619 (2010)
35. J. Chen, X. Zhou, C. Uher, X. Shi, J. Jun, H. Dong, Y. Li, Y. Zhou, Z. Wen, L. Chen, Acta Mater. **61**(5), 1508 (2013)
36. A.M. Adam, E. Lilov, P. Petkov, Superlattice. Microst. **101**, 609 (2017)
37. P. Nuthongkum, R. Sakdanuphab, M. Horprathum, A. Sakulkalavek, J. Electron. Mater. **46**(11), 6444 (2017)
38. C. Sudarshan, S. Jayakumar, K. Vaideki, C. Sudakar, Thin Solid Films **629**, 28–38 (2017)
39. M.-W. Jeong, S. Na, H. Shin, H.-B. Park, H.-J. Lee, Y.-C. Joo, Electron. Mater. Lett. **14**(4), 426 (2018)
40. Z.-K. Cai, P. Fan, Z.-H. Zheng, P.-J. Liu, T.-B. Chen, X.-M. Cai, J.-T. Luo, G.-X. Liang, D.-P. Zhang, Appl. Surf. Sci. **280**, 225 (2013)
41. P. Nuthongkum, A. Sakulkalavek, R. Sakdanuphab, J. Electron. Mater. **46**(5), 2900 (2017)
42. L.W. da Silva, M. Kaviany, Miniaturized thermoelectric cooler, in *ASME 2002 International Mechanical Engineering Congress and Exposition*, (American Society of Mechanical Engineers, New York, 2002), pp. 249–263
43. H. Zou, D.M. Rowe, S.G.K. Williams, Thin Solid Films **408**(1), 270 (2002)
44. L.W.d. Silva, M. Kaviany, C. Uher, J. Appl. Phys. **97**(11), 114903 (2005)
45. L.M. Goncalves, J.G. Rocha, C. Couto, P. Alpuim, M. Gao, D.M. Rowe, J.H. Correia, J. Micromech. Microeng. **17**(7), S168 (2007)
46. H. Bottner, J. Nurnus, A. Gavrikov, G. Kuhner, M. Jagle, C. Kunzel, D. Eberhard, G. Plescher, A. Schubert, K. Schlereth, J. Microelectromech. Syst. **13**(3), 414 (2004)
47. D.-H. Kim, E. Byon, G.-H. Lee, S. Cho, Thin Solid Films **510**(1), 148 (2006)
48. L.M. Goncalves, C. Couto, P. Alpuim, A.G. Rolo, F. Völklein, J.H. Correia, Thin Solid Films **518**(10), 2816 (2010)
49. G.J. Snyder, J.R. Lim, C.-K. Huang, J.-P. Fleurial, Nat. Mater. **2**, 528 (2003)
50. L.M. Gonçalves, The deposition of Bi_2Te_3 and Sb_2Te_3 thermoelectric thin-films by thermal co-evaporation and applications in energy harvesting, in *Thermoelectrics and its Energy Harvesting*, (CRC press, Boca Raton, 2012)
51. Z. Zhang, Y. Wang, Y. Deng, Y. Xu, Solid State Commun. **151**(21), 1520 (2011)
52. C.-L. Chen, Y.-Y. Chen, S.-J. Lin, J.C. Ho, P.-C. Lee, C.-D. Chen, S.R. Harutyunyan, J. Phys. Chem. C **114**(8), 3385 (2010)
53. H. Obara, S. Higomo, M. Ohta, A. Yamamoto, K. Ueno, T. Iida, Jpn. J. Appl. Phys. **48**(8R), 085506 (2009)
54. K. Choi, K. Jeong, J. Chae, H. Park, J. Baeck, T.H. Kim, J.Y. Song, J. Park, K.-H. Jeong, M.-H. Cho, Nano Energy **47**, 374 (2018)
55. M. Tan, Y. Hao, Y. Deng, D. Yan, Z. Wu, Sci. Rep. **8**(1), 6384 (2018)
56. M. Tan, Y. Hao, Y. Deng, J. Chen, Appl. Surf. Sci. **443**, 11 (2018)
57. F. Völklein, V. Baier, U. Dillner, E. Kessler, Thin Solid Films **187**(2), 253 (1990)
58. J. Tan, K. Kalantar-zadeh, W. Wlodarski, S. Bhargava, D. Akolekar, A. Holland, G. Rosengarten, Thermoelectric properties of bismuth telluride thin films deposited by radio frequency magnetron sputtering, in *Microtechnologies for the new millennium 2005*, (SPIE, Bellingham, 2005), p. 8
59. M. Tan, Y. Deng, Y. Wang, Nano Energy **3**, 144 (2014)
60. A. Foucaran, A. Sackda, A. Giani, F. Pascal-Delannoy, A. Boyer, Mater. Sci. Eng. B **52**(2), 154 (1998)

61. R.J. Mehta, Y. Zhang, C. Karthik, B. Singh, R.W. Siegel, T. Borca-Tasciuc, G. Ramanath, Nat. Mater. **11**(3), 233 (2012)
62. M.K. Jana, K. Biswas, C.N.R. Rao, Chem. Eur. J. **19**(28), 9110 (2013)
63. W. Wang, B. Poudel, J. Yang, D.Z. Wang, Z.F. Ren, J. Am. Chem. Soc. **127**(40), 13792 (2005)
64. G.-H. Dong, Y.-J. Zhu, L.-D. Chen, J. Mater. Chem. **20**(10), 1976 (2010)
65. G.-H. Dong, Y.-J. Zhu, L.-D. Chen, Cryst. Eng. Comm. **13**(22), 6811 (2011)
66. Y. Min, J. W. Roh, H. Yang, M. Park, S.I. Kim, S. Hwang, S.M. Lee, K.H. Lee, U. Jeong, Adv. Mater. **25**(10), 1425 (2013)
67. L.-D. Zhao, S.-H. Lo, Y. Zhang, H. Sun, G. Tan, C. Uher, C. Wolverton, V.P. Dravid, M.G. Kanatzidis, Nature **508**(7496), 373 (2014)
68. C. Chang, M. Wu, D. He, Y. Pei, C.-F. Wu, X. Wu, H. Yu, F. Zhu, K. Wang, Y. Chen, L. Huang, J.-F. Li, J. He, L.-D. Zhao, Science **360**(6390), 778 (2018)
69. L.-D. Zhao, C. Chang, G. Tan, M.G. Kanatzidis, Energy Environ. Sci. **9**(10), 3044 (2016)
70. G. Han, S.R. Popuri, H.F. Greer, J.-W.G. Bos, W. Zhou, A.R. Knox, A. Montecucco, J. Siviter, E.A. Man, M. Macauley, D.J. Paul, W.-g. Li, M.C. Paul, M. Gao, T. Sweet, R. Freer, F. Azough, H. Baig, N. Sellami, T.K. Mallick, D.H. Gregory, Angew. Chem. Int. Ed. **55**(22), 6433 (2016)
71. S. Chandra, A. Banik, K. Biswas, ACS Energy Lett. **3**(5), 1153 (2018)
72. S. Saha, A. Banik, K. Biswas, Chem. Eur. J. **22**(44), 15634 (2016)
73. Y. Luo, Y. Zheng, Z. Luo, S. Hao, C. Du, Q. Liang, Z. Li, K.A. Khor, K. Hippalgaonkar, J. Xu, Q. Yan, C. Wolverton, M.G. Kanatzidis, Adv. Energy Mater. **8**, 1702167 (2018)
74. Y. Ding, B. Xiao, G. Tang, J. Hong, J. Phys. Chem. C **121**(1), 225 (2016)
75. M.G. Kanatzidis, Acc. Chem. Res. **38**, 361 (2005)
76. M. Ruck, P.F. Poudeu Poudeu, Z. Anorg. Allg. Chem. **634**(3), 482 (2008)
77. M. Ohta, D.Y. Chung, M. Kunii, M.G. Kanatzidis, J. Mater. Chem. A **2**(47), 20048 (2014)
78. P.F. Poudeu, M.G. Kanatzidis, Chem. Commun. (21), 2672 (2005)
79. R. Atkins, M. Dolgos, A. Fiedler, C. Grosse, S.F. Fischer, S.P. Rudin, D.C. Johnson, Chem. Mater. **26**(9), 2862 (2014)
80. A. Mrotzek, M.G. Kanatzidis, Acc. Chem. Res. **36**(2), 111 (2003)
81. A. Mrotzek, M.G. Kanatzidis, J. Solid State Chem. **167**(2), 299 (2002)
82. L. Zhang, D. Singh, Phys. Rev. B **81**(24), 245119 (2010)
83. A. Chatterjee, K. Biswas, Angew. Chem. Int. Ed. **54**(19), 5623 (2015)
84. A. Banik, K. Biswas, Angew. Chem. Int. Ed. **56**(46), 14561 (2017)
85. L.E. Shelimova, O.G. Karpinskii, P.P. Konstantinov, E.S. Avilov, M.A. Kretova, V.S. Zemskov, Inorg. Mater. **40**(5), 451 (2004)
86. M.B. Babanly, E.V. Chulkov, Z.S. Aliev, A.V. Shevelkov, I.R. Amiraslanov, Russ. J. Inorg. Chem. **62**(13), 1703 (2017)
87. K. Nakayama, K. Eto, Y. Tanaka, T. Sato, S. Souma, T. Takahashi, K. Segawa, Y. Ando, Phys. Rev. Lett. **109**(23), 236804 (2012)
88. K. Yang, W. Setyawan, S. Wang, M.B. Nardelli, S. Curtarolo, Nat. Mater. **11**, 614 (2012)
89. M.G. Vergniory, T.V. Menshchikova, I.V. Silkin, Y.M. Koroteev, S.V. Eremeev, E.V. Chulkov, Phys. Rev. B **92**(4), 045134 (2015)
90. R. Vilaplana, J.A. Sans, F.J. Manjón, A. Andrada-Chacón, J. Sánchez-Benítez, C. Popescu, O. Gomis, A.L.J. Pereira, B. García-Domene, P. Rodríguez-Hernández, A. Muñoz, D. Daisenberger, O. Oeckler, J. Alloys Compd. **685**, 962 (2016)
91. A.M. Kusainova, P.S. Berdonosov, L.G. Akselrud, L.N. Kholodkovskaya, V.A. Dolgikh, B.A. Popovkin, J. Solid State Chem. **112**(1), 189 (1994)
92. S.D.N. Luu, P. Vaqueiro, J. Materiomics **2**(2), 131 (2016)
93. L.-D. Zhao, J. He, D. Berardan, Y. Lin, J.-F. Li, C.-W. Nan, N. Dragoe, Energy Environ. Sci. **7**(9), 2900 (2014)
94. M. Samanta, S.N. Guin, K. Biswas, Inorg. Chem. Front. **4**(1), 84 (2017)
95. L. Yang, Z.-G. Chen, G. Han, M. Hong, Y. Zou, J. Zou, Nano Energy **16**, 367 (2015)
96. H. Liu, X. Shi, F. Xu, L. Zhang, W. Zhang, L. Chen, Q. Li, C. Uher, T. Day, G.J. Snyder, Nat. Mater. **11**(5), 422 (2012)